ACS OMEGA

Article

Cite This: ACS Omega 2018, 3, 18420−18432

http://pubs.acs.org/journal/acsodf

# Femtosecond Laser-Induced, Nanoparticle-Embedded Periodic Surface Structures on Crystalline Silicon for Reproducible and Multi-utility SERS Platforms

Syed Hamad,[†] Sree Satya Bharati Moram,[†] Balaji Yendeti,[†] G. Krishna Podagatlapalli,[†,#] S. V. S. Nageswara Rao,[‡] Anand Prakash Pathak,[‡,▽] Mahamad Ahamad Mohiddon,[§,⊥] and Venugopal Rao Soma*[,†]

[†]Advanced Centre of Research in High Energy Materials (ACRHEM), University of Hyderabad, Hyderabad, Hyderabad 500046, Telangana, India

[‡]School of Physics, University of Hyderabad, Hyderabad 500046, Telangana, India

[§]Centre for Nanoscience and Technology, University of Hyderabad, Prof. C. R. Rao Road, Gachibowli, Hyderabad 500046, India

**ABSTRACT:** Fabrication of reproducible and versatile surface-enhanced Raman scattering (SERS) substrates is crucial for real-time applications such as explosive detection for human safety and biological imaging for cancer diagnosis. However, it still remains a challenging task, even after several methodologies were developed by various research groups, primarily due to (a) a lack of consistency in detection of a variety of molecules (b) cost-effectiveness of the SERS substrates prepared, and (c) byzantine preparation procedures, etc. Herein, we establish a procedure for preparing reproducible SERS-active substrates comprised of laser-induced nanoparticle-embedded periodic surface structures (LINEPSS) and metallization of silicon (Si) LINEPSS. LINEPSS were fabricated using the technique of femtosecond laser ablation of Si in acetone. The versatile SERS-active substrates were then achieved by two ways, including the drop casting of silver (Ag)/gold (Au) nanoparticles (NPs) on Si LINEPSS and Ag plating on the Si LINEPSS structures. By controlling the LINEPSS grating periodicity, the effect of plasmonic nanoparticles/plasmonic plating on the Si NPs embedded periodic surface structures enormously improved the SPR strength, resulting in the consistent and superior Raman enhancements. The reproducible SERS signals were achieved by detecting the molecules of Methylene Blue (MB), 2,4-dinitrotoluene (DNT), and 5-amino-3-nitro-l,2,4-triazole (ANTA). The SERS signal strength is determined by the grating periodicity, which, in turn, is determined by the input laser fluence. The SERS-active platform with grating periodicity of 130 ± 10 nm and 150 ± 5 nm exhibited strong Raman enhancements of ∼$10^8$ for MB and ∼$10^7$ for ANTA molecules, respectively, and these platforms are demonstrated to be capable, even for multiple usages.

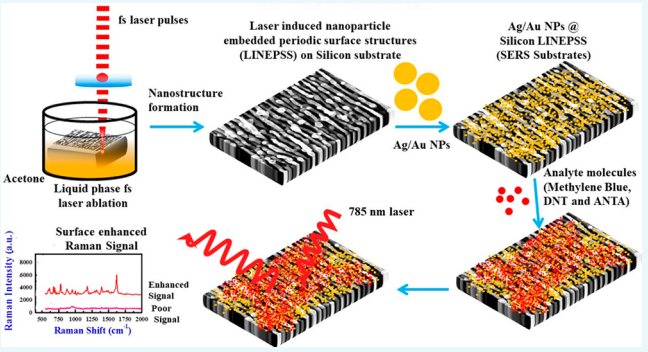


## INTRODUCTION

In the present scenario of prevailing terror activities, the security of personnel and the important infrastructure has gained significance worldwide (e.g., to avert encounters from terrorist activities), and efforts are directed toward overcoming the ineptitude of existing diagnostic tools, including obliteration of health hazards (e.g., early stage detection of cancer, trace level detection of bacteria).[1−3] One of the possible solutions for the above-mentioned problems is the development of detection techniques and improvisation of diagnostic limits incorporating advanced technologies. With the fast development of spectroscopy techniques, standoff and near-field detection studies have been established by various groups for the detection of explosives. However, there is no such universal technique that is capable of detecting diverse explosives positively in a single experiment. Some spectroscopic methods that have been extensively studied to identify explosive molecules involve either tedious processes or require expensive equipment. Among many such detection techniques, spectroscopic tools that incorporate Raman scattering as the key element are efficient and practical, since these are versatile for explosives detection and health diagnostics.[4] Raman spectroscopy is an excellent technique that works both in near field and standoff modes, especially for explosives detection. Although spontaneous Raman scattering techniques demonstrate significant molecular finger prints, it cannot accomplish trace level detection, because of its very small scattering cross-section (∼$10^{-36}$ $cm^2$/molecule). In 1974, Fleischman et al.[5] experimentally demonstrated the first Raman signal enhancements (5 to 6 orders) of pyridine

Received: October 2, 2018
Accepted: December 18, 2018
Published: December 27, 2018

molecules adsorbed on a coarsened silver electrode, which was later named as surface-enhanced Raman scattering (SERS). In SERS, any molecule in the close vicinity (<4 nm) of a nanomaterial experiences the fourth power of local electric field by the excitation of surface plasmons. As a result, polarizability of the molecule is enhanced and, hence, the Raman scattering cross section increases gigantically. SERS has now become an extensively investigated hot topic, and developments have reached a highpoint that this technique is now capable even to detect/identify single molecules. The single molecular (SM) detection was performed by two individual groups Kneipp et al. and Nie et al.[6,7] They described the gigantic evanescent fields as being due to the hot spots, which are rederived from the combined localized surface plasmon resonances, produced between the junctions of nanoparticles. The Raman signal intensity is extremely influenced by the morphological/topographical aspects of a nanomaterial such as size, shape, and uniformity of the nanostructure on the substrate, which affect the reproducibility of SERS signal from a SERS-active platform.[8] Plasmonic metal plating (or) nanoparticles coated on nanoporous semiconductors[9] (or) patterned dielectric substrates[10] were synthesized by chemical and physical methods. These substrates have received strong attention and became hot areas in SERS, which could demonstrate huge Raman signal enhancements. However, the reproducibility factor, less consistency, great sensitivity, and detection efficiency have been important factors limiting the SERS applications for large-area detection. To maximize the reproducibility factor of the SERS-active substrate with the largest uniformity, various methods have been implemented to produce nanostructures with high uniformity. These methods include dual interference lithography,[11] high-resolution electron beam lithography,[12] ion beam lithography,[13] anodic aluminum oxide template-assisted electrochemical deposition,[14] electroless etching,[15] and ultrafast laser ablation technique.[16] Such methods are capable to generate large-area uniform SERS-active substrates. Versatile SERS-active substrates are urgently required for real-time applications, such as trace level detection of explosives[17,18] and imaging of microorganisms.[19] Nanoaggregation of plasmonic metals (or) nanoparticles dispersed on plasmonic metal sheet provides irregularities and offer randomly distributed hotspots because of the coupling of metal nanostructures/nanoparticles, leading to huge random SERS enhancement. Scientists confirmed that SERS enhancement was obtained[17] because of randomly oriented hotspots is more than the enhancement obtained in the case of roughened/corrugated nanostructures[20,21] and individual nanoparticles (NPs) of traditional plasmonic metals (Au, Ag, and Cu).[22,23] However, the substrates with randomly oriented hot spots may not serve as uniform SERS-active substrates, because of the lack of homogeneity in the Raman signals recorded from different locations of the SERS-active platform. To address the issue of homogeneity and reproducibility of SERS signal, periodic nanostructures are the most suitable candidates and a sensible investigation was done by some researchers.[24−29] Pioneers of the field fabricated large-area ridged hexagonal nanostructures using interference lithography and demonstrated reproducible SERS with tenability.[11] Yokota et al.[12] have recently reported the SERS studies of crystal violet molecules at ultralow concentrations in the vicinity of highly controlled nanoengineered Au square blocks using high-resolution electron lithography. The anodic aluminum oxide (AAO) deposition method was utilized to generate large-area gold-nanoparticle-coated polymer pillar arrays for reproducible and significant SERS enhancement.[30] The R2R UV-NIL and AAO techniques were employed to fabricate continuous cost-effective polymer nanostructure arrays, and these substrates have shown SERS enhancement for R6G molecule on the order of $10^7$.[31] However, all of the above-mentioned methods are quite cumbersome, time-consuming with low throughput, and highly expensive. At the same time, the residual chemical contents remain on the surface of the nanomaterial, which are very difficult to get rid of completely. In order to overcome the difficulties posed by the other well-known methods of nanomaterial fabrication, ultrafast laser ablation is one of the simple and time-saving top-down approaches to green synthesis.

Femtosecond (fs) laser ablation is a powerful tool to fabricate microstructures and nanostructures for biomedical,[32−34] wettability,[35] and photonics applications.[36] Focusing an ultrafast laser beam at the liquid/material interface helps to engineer the desired nanomaterials with required shapes, as a function of the influence of liquid parameters (viscosity, polarity, etc.), laser fluence, and pulse number. The fs laser irradiation/ablation technique offers laser-induced periodic surface structures (LIPSS) on the surface of every material, such as metals,[37−39] semiconductors,[40−42] and dielectrics.[43−45] In fs direct writing, many techniques have been developed to optimize the fabrication process and generate nanostructures with size lower than the diffraction limit.[46−49] Fadeeva et al.[50] reviewed biomimetic liquid-repellent surfaces via ultrafast laser processing and summarized the modifications of different materials (metals, semiconductors, and polymers). There are some reports that demonstrated the randomly aligned and well-controlled surface structures. In the last two decades, several mechanisms behind the formation of LIPSS have been proposed by researchers.[51−62] First, LIPSS are formed due to the interference of incident wave and surface electromagnetic wave propagating along the ablated surface.[63] Second, when light interacts with porous surface of the material, it introduces a scaling factor that arises due to nonuniform energy distribution of the ultrafast laser pulse on the ablated surface. This leads to a nonuniform absorption of pulse energy and consequently generates LIPSS.[56] The later theory (or) mechanism, along with surface electromagnetic wave (or) plasmon polaritons wave concepts, was universally accepted by many research groups. Unlike nanoparticles, LIPSS offer extraordinary applications, such as those in optical data storage, color displays, hydrophobic/hydrophilic, wetting, bacterial cell (or) any other cell growth, SERS, and many industrial fields. Particularly, the esteemed application of LIPSS substrates is that they act as SERS-active platforms with very significant features, which cannot be seen in other contemporary SERS platforms. The processing of LIPSS on semiconductors (or) dielectrics and eventually gold/silver plating on them can be extensively used as SERS-active substrates. In contrast, LIPSS processing on plasmonic materials (gold,[51] silver) have not been studied extensively, because of their partially compatible thermophysical properties. The main reason behind the low priority of LIPSS processing on Au and Ag, when compared with semiconductors and dielectrics, especially concerns the electronic configuration of plasmonic materials, which anticipate low electron−phonon coupling constant.[64] Electron−phonon coupling constant plays a unique role in the formation of


DOI: 10.1021/acsomega.8b02629
ACS Omega 2018, 3, 18420−18432

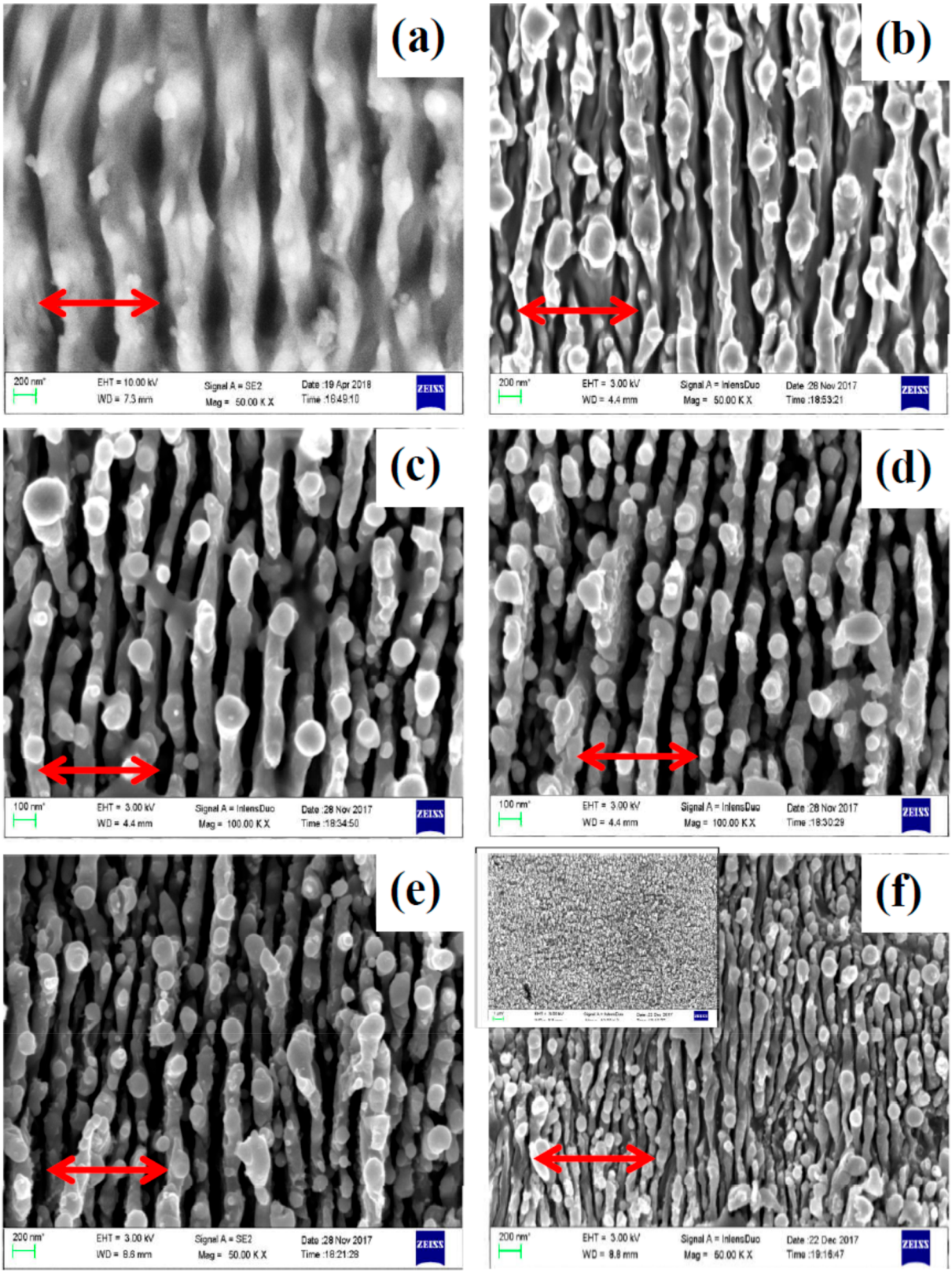


**Figure 1.** FESEM images of laser-ablated regions on crystalline Si in acetone (a) high-special-frequency LIPSS (HSFL) formed at a fluence of 0.08 J/cm$^2$; (b, c, d, e) clear view of nanoparticle-embedded LIPSS produced at 0.19 J/cm$^2$, 0.38 J/cm$^2$, 0.75 J/cm$^2$, 1.5 J/cm$^2$; and (f) disjointed LIPSS at 3 J/cm$^2$ and its inset shows the lower-magnification image (1 $\mu$m scale bar). Arrow marks depict the laser beam polarization direction.

nonuniform energy distribution on the surface of the material, which leads to LIPSS. Thus far, various groups have demonstrated LIPSS processing on silicon substrate using the fs ablation/writing technique[40,41,47,48,57,65,66] and few groups confirmed that the Ag/Au plating on silicon LIPSS can also be used as very good SERS-active substrates.[67]



DOI: 10.1021/acsomega.8b02629
*ACS Omega* 2018, 3, 18420−18432

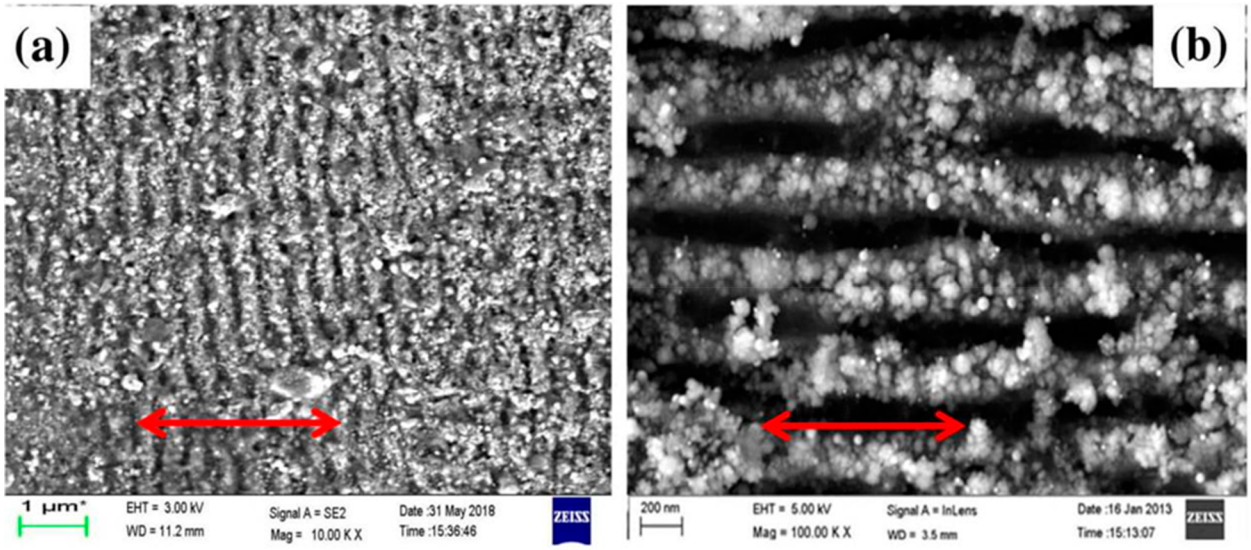


**Figure 2.** FESEM images of laser-ablated regions on crystalline Si in air: (a) low-special-frequency LIPSS (LSFL) formed with 20 pulses per spot and (b) high-special-frequency LIPSS (HSFL) formed with ∼700 pulses at a fluence of 0.38 J/cm$^2$. Arrow indicates the laser beam polarization direction.

Moreover, Ag coated on randomly formed silica NSs by fs ablation technique was explored as SERS-active substrates.[68] Yang et al.[16] have reported the fs laser fabricated microstructures/nanostructures on Si wafer, coated with Ag layer through thermal deposition for SERS detection of biomolecules. Zhu et al.[69] have proposed a quick and straightforward method to fabricate large-area SERS-active Si substrates by fs laser pulses, which were covered with Au thin film and demonstrated an enhancement factor an order of $10^7$ in the case of R6G molecule. In the current work, we demonstrate the fabrication of a new SERS substrate including laser-induced nanoparticles embedded in periodic surface structures (LINEPSS) on Si substrate and Ag/Au metallization of Si nanostructures. These Si structures were produced using fs pulses and appropriate fluences that facilitate the processing of localized surface structures on silicon, i.e., submerged in a liquid medium. The productive SERS-active substrates are then acquired by plasmonic NPs deposited by drop casting/plasmonic plating on LINEPSS using an ion beam deposition method. In fact, this unique SERS substrate is able to provide various hotspots at once, which result in the formation of high electromagnetic field sites and therefore produce a huge enhancement in the signal. In generic SERS-active platforms, NPs support the localized surface plasmons (LSPs). In the present case, (i) the dispersed Ag/Au NPs on LINEPSS substrate allow the creation of a higher number/multiple hotspots, which support strong localized surface plasmons and lead to a higher enhancement in the SERS signal; (ii) Ag-film-coated LINEPSS substrate permit excitation of both localized surface plasmons and propagating surface plasmons (PSPs), which tremendously enhances the local field and, consequently, the Raman signal. This could be the advantage of LINEPSS compared to ordinary SERS-active platforms. Furthermore, uniformity and stability of the fabricated LINEPSS substrates have been investigated for their reproducibility and multiple utility SERS measurements. This study can possibly yield an effective way for the fabrication of uniform SERS-active substrates.

## RESULTS AND DISCUSSION

In order to fabricate the surface nanostructures, we have performed fs ablation of Si in acetone at different fluences much more beyond the limit of ablation threshold ($F_{th}$ = 0.3 J/cm$^2$). The results presented in Figure 1 illustrate the size/shape variation of Si nanostructures, depending on the laser fluence. Figures 1a−f represent the FESEM micrographs for laser-machined Si substrates with various fluences, ranging from 0.08−3 J/cm$^2$ in acetone for 30 min. These images demonstrate the formation of high-spatial-frequency LIPSS (HSFL) structures on the Si(100) substrate. By considering 300 lines from SEM images in each case,[16,17,19−22] the average periodicity of HSFL structures on the Si substrate was estimated to be 350 ± 20 nm, 285 ± 15 nm, 130 ± 10 nm, 150 ± 5 nm, 200 ± 30 nm, and disjointed LIPSS for 0.08 J/cm$^2$, 0.19 J/cm$^2$, 0.38 J/cm$^2$, 0.75 J/cm$^2$, 1.5 J/cm$^2$, and 3 J/cm$^2$, respectively. A plausible mechanism for the formation of LIPSS structures on a solid surface is the absorption and relaxations of the carrier density with excitation of fs pulses in liquid media. Various scattering effects can also be observed at different time scales. When the fs pulses interact with acetone-immersed Si, the energy of the leading part is principally deposited on Si at the liquid/material interface and Si absorbs the energy by inverse Bremsstrahlung[70,71] through the two-photon (or) multiphoton absorption process within the period of ∼10−100 fs at higher peak intensities. The excited electrons collide with each other (or) with bounded electrons, resulting in the production of high electron density in Si which approaches close to the critical electron density of Si. The same kind of behavior can be expected in acetone, because of the optical Kerr effect at similar high peak intensity. Under these conditions, the optical properties of both materials (acetone and Si) are modified to a great extent and acquire almost metallic behavior[72,73] at the liquid/material interface. Later on, the trailing part of the ultrafast laser pulse interacts with the material melt, which has acquired the metallic behavior.

The interaction of the trailing part with the melt excites the possible plasmonic modes, leading to the generation of surface



DOI: 10.1021/acsomega.8b02629
ACS Omega 2018, 3, 18420−18432

plasmon polaritons (SPP).[72,73] The generated SPP waves interfere with incident electromagnetic wave and produces LIPSS on the Si surface. As per the literature, the interference mechanism could be more suitable to the formation of low-spatial-frequency LIPSS (LSFL) structures in an air medium, described successfully by many scientists based on Drude–Sipes theory. According to this theory, Huang et al.,[74] Bonse et al.,[40,53] and Sipe et al.[56] have explained the orientation of polarization and characteristics of LSFL structures. The physical mechanism behind the formation of HSFL in air is still being debated.

Figure 2 illustrates the FESEM images of (a) LSFL structures and (b) HSFL structures (with large number of pulses) formed on silicon on silicon in air at ∼0.38 J/cm$^2$ fluence. As observed from Figures 1c and 2b, both HSFL structures in acetone and air are having different orientation of surface structures (polarization) with different periods. In the case of acetone, HSFL with a periodicity ∼130 nm is generated and their orientation is perpendicular to the incident field polarization. In air, HSFL nanostructures with a periodicity of ∼370 nm are generated with an orientation that is parallel to the incident field polarization. It was observed that the orientation of HSFL structures in liquid media is more similar to LSFL structures (Figure 2 a, 700 nm) orientation (perpendicular to incident field polarization direction) in air.[75] This similarity could be due to the same physical mechanism process occurring during the production of HSFL structures in liquid and LSFL structures in air. Miyaji et al.[73] proposed an SPP wave model for HSFL formation in liquid media. In addition, we observed the deposition of Si nanoparticles on LIPSS structures in Figures 1c–e when the fluences were greater than the ablation threshold of the Si. We obtained average sizes of the Si nanoparticles using SEM image and image J software, wherein we have taken at least 250 nanoparticles from 4 SEM images. The mean size of Si NPs are estimated to be ∼150 nm, ∼90 nm, ∼67 nm, ∼135 nm, and ∼95 nm for 0.19 J/cm$^2$, 0.38 J/cm$^2$, 0.75 J/cm$^2$, 1.5 J/cm$^2$, and 3 J/cm,[2] respectively. At higher fluences, plasma generation occurs at a particular stage and expands to generate the shock wave. During the development of a shock wave, the expansion of plasma in the plume form moves into the surrounding liquid media and it gets quenched within the time scale of 100 ns,[76] resulting in the formation of a cavitation bubble. The bubble follows a radial motion, because of its sinusoidal driving pressure.[77] When the rarefaction part of the pressure field interacts with medium, the cavitation bubble increases in size, which increases the pressure inside the bubble, compared to the surrounding pressure.[78] As in the case of the compression part, the size of the bubble slightly decreases, because of the slow pressure increase inside the bubble. After a few microseconds, the continuous cavitation bubble grows in the form of compression and rarefaction. During the bubble growth, the bubble contains nanosized ablated material.[76,79] However, the rapid growth of the bubble, followed by collapse, typically occurs within a time scale of 10–300 $\mu$s. During the expansion of CB into the surrounding liquid, the medium exerts a gigantic pressure on the metallic plume. This recoil pressure splashes the metal plume into nanoparticles. Transient dynamics of the plasma can prompt composite material fabrication, because of its interaction with the liquid medium surrounding it.[80–83] Subsequently, the vaporized material fragments resolidify (generation of NPs) over a time scale of few hundreds of microseconds. During the process of (CB's) expansion, the temperature gradient in the inner and outer surfaces of the CB leads to condensation and growth of NPs. The produced nanoparticles slow their velocity by losing their kinetic energy during the collision with other species or clusters, and some of them end up landing on Si LIPSS, because of van der Waals forces and form the LINEPSS. It is familiar that laser ablation of Si in air and water at higher fluences produced $SiO_2$ on the surface of the Si.[16]

Figure 3 shows the Raman spectrum of ablated Si substrates at different fluences of 0.08–3 J/cm$^2$ in acetone for 30 min,

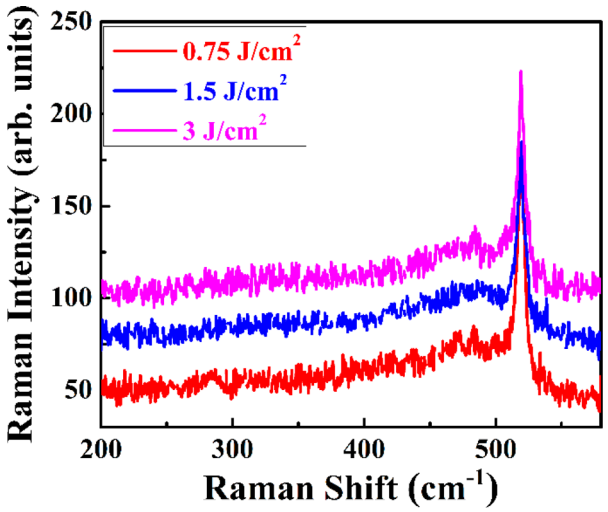


**Figure 3.** Raman spectra of patterns on the Si substrates demonstrating an amorphous peak near 480 cm$^{-1}$ and asymmetric crystalline peak at 519 cm$^{-1}$.

which demonstrate crystalline nature of the Si nanostructures. In the Raman spectrum, mainly a broad peak at 518 cm$^{-1}$ was observed, along with 470 cm$^{-1}$ peak, which confirmed the formation of nanocrystalline and nanoamorphous Si on the ablated surface. In order to interpret the constituents on the Si surface after the ablation of Si in acetone, energy-dispersive X-ray (EDAX) analysis of Si LINEPSS structures fabricated at different fluences (0.08 J/cm$^2$, 0.19 J/cm$^2$, 0.38 J/cm$^2$, 0.75 J/cm$^2$, 1.5 J/cm$^2$, and 3 J/cm$^2$) have been executed in FESEM system (at 5 eV), as shown in Figure 4. The EDAX data demonstrated that lower and higher fluences induce the minimal oxidation and this oxidation does not affect the SERS efficiency.

Figure 5 illustrates the EDAX spectra of Ag nanoparticles (∼15 nm) (Figure 5a) and Au nanoparticles (∼10 nm) (Figure 5b) deposited on LINEPSS structures, revealing peaks corresponding to Ag/Au and Si in all cases. The morphology of Ag and Au colloidal NPs were reported by our group in earlier articles.[84] This certifies that Ag/Au NPs and Si NPs were successfully observed without any significant impurities. Figures 5c and 5d illustrate the EDAX and FESEM images of Ag film deposited on Si LINEPSS structures fabricated at a fluence of 0.75 J/cm$^2$, respectively. The EDAX spectra of Ag film deposited on Si LINEPSS structures exhibit Ag and Si peaks. As seen in Figure 5d, the shape of film is irregular and formed as Ag islands on Si LINEPSS. These Ag island-shaped films on Si NPs allow to produce localized surface plasmons and nanoroughness on Si grating NSs may lead to the excitation of propagating surface plasmon and the combined


DOI: 10.1021/acsomega.8b02629
ACS Omega 2018, 3, 18420–18432

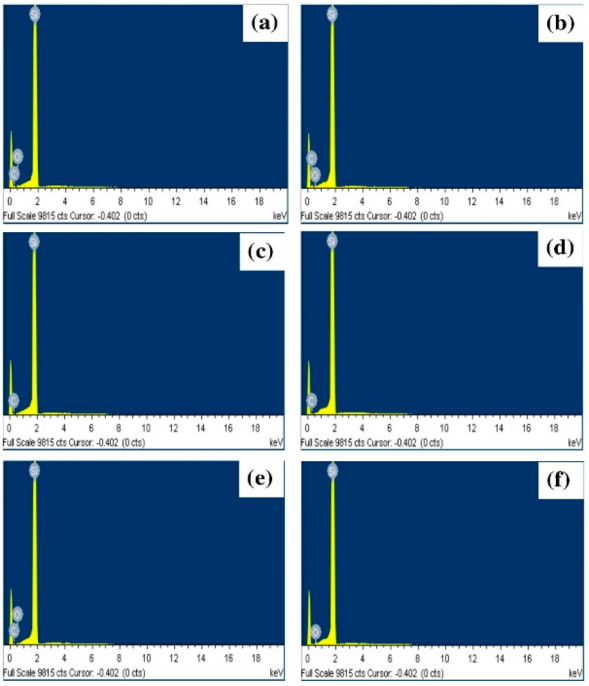


**Figure 4.** EDX spectra of ablated portions on crystalline Si in acetone at a fluence of (a) 0.08 J/cm$^2$, (b) 0.19 J/cm$^2$, (c) 0.38 J/cm$^2$, (d) 0.75 J/cm$^2$, (e) 1.5 J/cm$^2$, and (f) 3 J/cm$^2$, demonstrating minimal oxidation effect on the substrates.

effect of localized and propagating surface plasmons leads to a strong SERS signal.

**SERS Performance of the Substrates.** It is obvious from the earlier reports on the SERS measurements that the excitation of nontransparent hybrid plasmonic (or) plasmonic nanostructures with 785 nm is beneficial when compared to other excitation wavelengths, since they possess higher surface plasmons at 785 nm. In this study, laser Raman portable system with a beam diameter of 0.2 mm and an excitation wavelength of 785 nm is utilized to acquire SERS spectra of all the substrates. The efficiency of SERS-active hybrid nanostructures was exploited by means of enhancement in Raman signal obtained from Methylene Blue (MB). As mentioned in the past research, enhancement in Raman signal of substrates is related to different groove depths of Si micrograting.[67] To study the influence of LIPSS periodicity on the Raman signal enhancement, SERS spectra of Ag (~15 nm) deposited onto Si LINEPSS with different periodicity were recorded and are shown in Figure 6a. As seen in Figure 6a, there are three prominent Raman bands observed at 447, 1393, and 1620 cm$^{-1}$ in all SERS spectra, which are well-matched with reported MB characteristic Raman peaks,[84,85] and these modes correspond to C−N−C skeletal deformation, C−N symmetrical stretch, and C−C ring stretching, respectively. In addition, other vibrational modes were also observed at 770, 1037, 1161, and 1500 cm$^{-1}$, which is an observation that is consistent with other Raman bands of MB. As illustrated in Figure 6a, the Raman peak intensity amplifies as the periodicity decreases from 350 ± 20 nm to 130 ± 10 nm and then the intensity starts decreasing at 150 ± 5 nm and further signal intensity decreases when the LINEPSS structure gets extracted.

Among all the SERS-active substrates, substrate with LINEPSS and periodicity of 130 ± 10 nm demonstrated a superior SERS signal, which could be due to a greater number of Ag nanoparticles dispersed on the LINEPSS structure, and this condition allows MB molecules to be adsorbed on Ag NPs in large numbers, because of the large uniform substrate. Under these circumstances, the almost-dispersed Ag nanoparticles on the LINEPSS substrate allows the creation of more multiple hotspots, which might lead to strong enhancement of the evanescent electric field. As in the case of larger periodicity of LINEPSS, Ag NPs dispersed on the LINEPSS substrate might decrease and the distance between two Ag NPs could be small and, hence, represent a smaller number of hotspots, which boosts the enhancement of local field significantly. However, the substrate with disjointed LINEPSS generates a very low SERS signal, which could be accredited to the lower density of the Ag NPs that cover the Si LINEPSS substrate, and this results in minimal hotspots. Hence, our studies demonstrated that Ag NPs covered on LINEPSS with a periodicity of 130 ± 10 nm is the most favorable substrate for SERS enhancement. In comparison, the substrate with Ag NPs on plain Si exhibited very small signal strength and this small

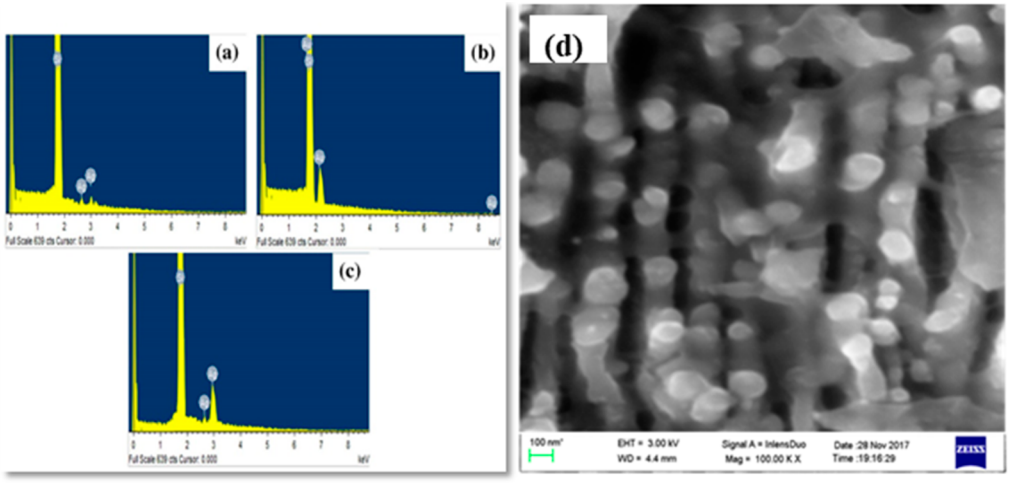


**Figure 5.** (a) EDAX spectra of Ag NPs deposited LINEPSS Si substrate, (b) EADX spectra of Au NPs deposited LINEPSS Si substrates, and (c) EADX spectra of Ag plating on LINEPSS Si substrates produced at a fluence of 0.38 J/cm$^2$, illustrating the respective Si, Ag, and Au peaks, and (d) FESEM image of Ag plating on Si LINEPSS substrate fabricated at 0.75 J/cm$^2$.



DOI: 10.1021/acsomega.8b02629
ACS Omega 2018, 3, 18420−18432

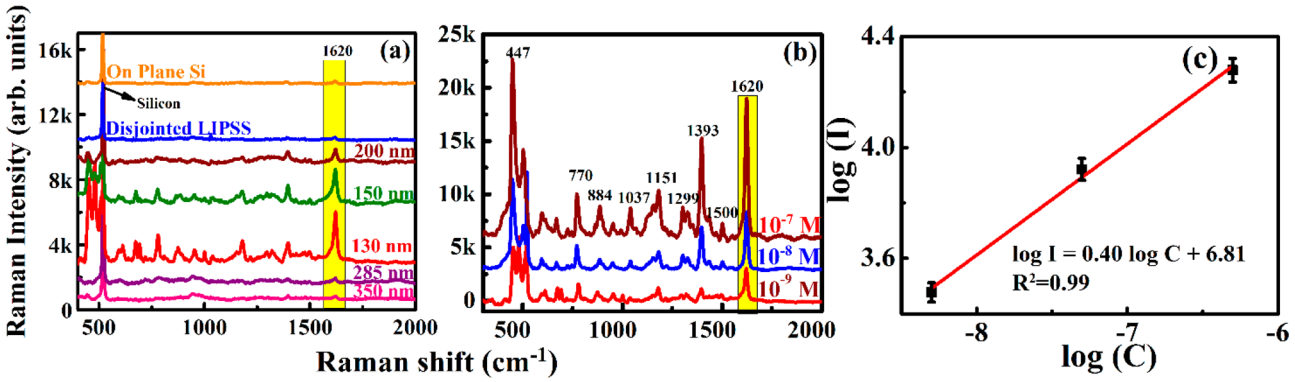


**Figure 6.** SERS spectra of MB ($10^{-9}$ M) absorbed on (a) Ag-NPs-coated LINEPSS substrates with different periodicity, recorded with 785 nm portable Raman system with 5 mW power and the integration time was 5 s for each spectrum and (b) different concentration (increasing) Ag-NPs-coated LINEPSS substrate with 130 ± 10 nm, recorded with 785 nm portable Raman system with 5 mW power and the integration time was 5 s for each spectrum. The main characteristic peak is highlighted in yellow. (c) The linear relationship of log *C* vs log *I*, demonstrating a $R^2$ value of 0.99.

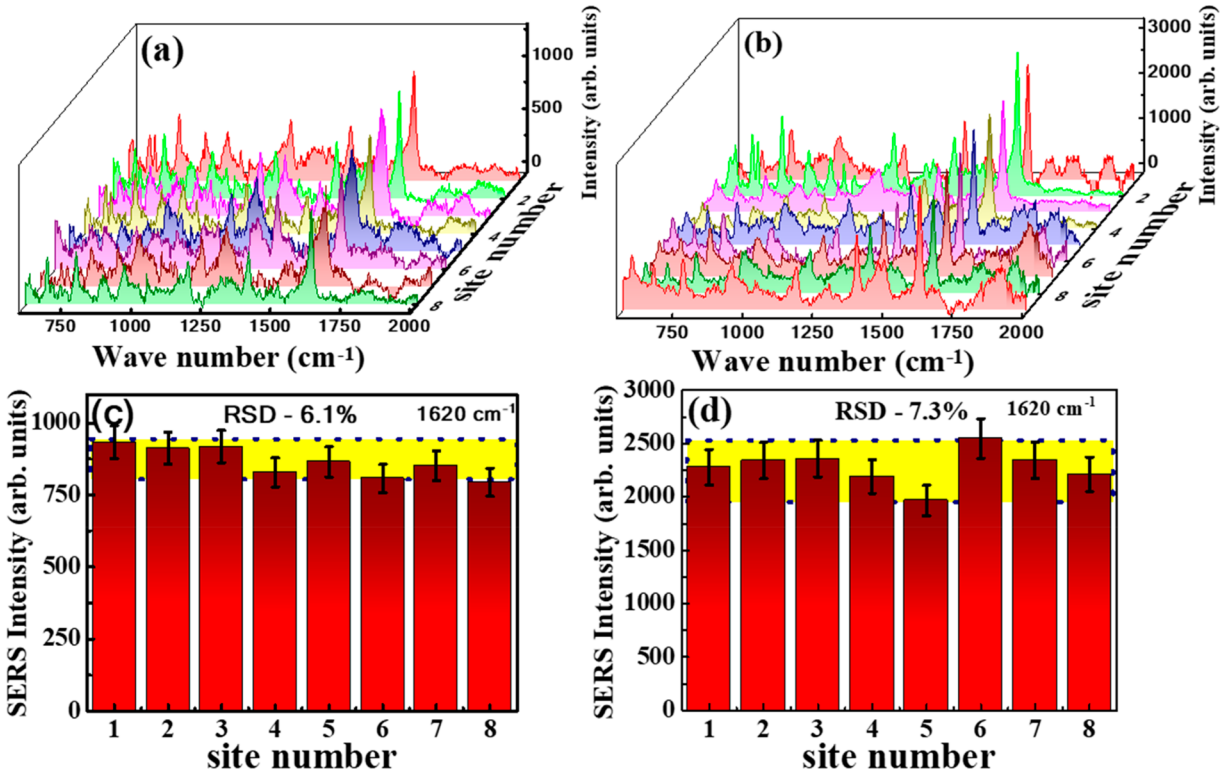


**Figure 7.** SERS spectra of MB ($10^{-9}$ M) absorbed on Ag-NPs-coated LINEPSS substrates recorded from eight positions from LINEPSS substrates with a periodicity of (a) 150 ± 10 nm and (b) 130 ± 5 nm. A 785-nm portable Raman system with 5 mW of power was used and the integration time was 5 s for each spectrum. (c, d) Corresponding reproducibility data for the 1620 $cm^{-1}$ peak.

signal could be due to the lesser number of hotspots (or) individual surface plasmon effect. The SERS enhancement obtained is ∼100 times lower for Ag NPs on plain Si substrate, when compared to the enhancement obtained in the case of LINEPSS with a periodicity of 130 ± 10 nm. Figure 6b illustrates SERS spectra of MB molecules of different concentrations adsorbed on LINEPSS with a periodicity of 130 ± 10 nm and it is demonstrated that the SERS signal intensity increased with MB concentration. As is evident from the data presented in Figure 6b, a considerable intensity was observed, even at lower concentration ($10^{-9}$), confirming the highly sensitive nature of the present SERS substrate. Figure 6c illustrates a log−log plot of SERS intensity versus the concentration of MB, and the data obtained established a linear relationship with the increasing concentration of MB molecule.

To explore the enhancing capability of Ag-NPs-covered LINEPSS substrates, the enhancement factor (EF) in each case was evaluated by comparing the SERS intensity of the molecule with normal Raman intensity of same molecule (MB in this case) on plain Si surface using the formula[21]

$$\mathrm{EF} = \frac{I_{\mathrm{SERS}}/I_{\mathrm{Raman}}}{N_{\mathrm{SERS}}/N_{\mathrm{Raman}}}$$

Here, $I_{\mathrm{SERS}}$ and $I_{\mathrm{Raman}}$ refer to the Raman peak intensities of MB molecule at a 1 nM concentration ($C_{\mathrm{SERS}}$) on the SERS-active substrate and a 0.1 M concentration ($C_{\mathrm{ref}}$) on the pure Si substrate, respectively. $N_{\mathrm{SERS}}$ and $N_{\mathrm{Raman}}$ represent the number



DOI: 10.1021/acsomega.8b02629
ACS Omega 2018, 3, 18420−18432

of molecules contributing to the enhancement of Raman intensity and normal Raman intensity, respectively. In the present study, we estimated the EF values for the characteristic mode (1620 $cm^{-1}$) of MB and found them to be $6.7 \times 10^6$, $9.3 \times 10^6$, $1.5 \times 10^8$, $7.8 \times 10^7$, $3 \times 10^7$, and $5 \times 10^6$ for LINEPSS substrates with a periodicity of 350 ± 20 nm, 285 ± 15 nm, 130 ± 10 nm, 150 ± 5 nm, 200 ± 30 nm, and disjointed LIPSS, respectively. In our investigation, the highest EF value was evaluated to be $1.5 \times 10^8$, which could be lower than the other's reported EF value for MB on the other substrates, such as Ag−Au alloy nanoparticles[86] and Ag NPs deposited porous Si.[87] Hamdorf et al.[88] fabricated three-dimensional (3D) large-area microstructures/nanostructures on silicon substrate in three steps: (i) fs laser micromachining and roughening, followed by (ii) thin-film coating and (iii) nanosecond laser heating and melting. This 3D substrate provided an enhancement that was 100 times higher than the EF value obtained in the case of a flat substrate. Other researchers have confirmed that SERS efficiency changes under the influence of size and shape of nanostructures, and a large uniform SERS-active substrate can be utilized for the detection of more than two probe molecules at a time.[89,90] Our group recently reported that the multiple utility of nanostructures for the trace detection of organic molecules has been handled with a simple cleaning process.[21] Although the cleaning process was gentle, it could possibly affect the surface morphology of the NSs and, hence, affect the SERS performance. However, if the substrate is efficient enough, one could achieve significant enhancements, even after a second and third cleaning procedure, as was demonstrated earlier by our group.[21] The reproducibility of the Raman peak intensities of analyte molecules adsorbed on SERS-active substrates is a prerequisite for real-time practical applications. For the confirmation of reproducibility behavior in our substrate, we have recorded the SERS spectrum of MB ($10^{-9}$ M) in eight different locations on LINEPSS substrates with 130 ± 10 nm and 150 ± 5 nm, and found identical intensities, as illustrated in the data of Figures 7a and 7b, respectively. Figures 7c and 7d demonstrate the histogram plots for major Raman peak on two LINEPSS substrates with 130 ± 10 nm and 150 ± 5 nm, and we estimated the relative standard deviation (RSD) in both cases to be <8%. The RSD values of <10% have confirmed that our substrates can be utilized for practical applications. Subsequently, the above-mentioned two substrates, such as the LINEPSS substrates with a periodicity of 130 ± 10 nm and 150 ± 5 nm, with Ag NPs, were employed again for the SERS measurements of 2,4-dinitrotoluene (DNT), following a sonication procedure in acetone. Figure 8 illustrates the SERS spectra of DNT molecules recorded with a concentration of $10^{-6}$ M collected from two LINEPSS substrates (130 ± 10 nm and 150 ± 5 nm) dispersed with Ag NPs. The SERS spectra clearly illustrate the peaks at 856 and 1344 $cm^{-1}$, corresponding to $NO_2$ out-of-plane mode and $NO_2$ symmetric stretch mode, respectively.[91] We assumed that 30%−40% of the analyte molecules were adsorbed on substrates. The estimated EF values for LINEPSS substrates with a periodicity of 130 ± 10 nm and 150 ± 5 nm, and with Ag NPs, were $4.9 \times 10^5$ and $1.6 \times 10^5$, respectively.

**Multiple Utility of Substrates.** The efficient SERS substrates should exhibit exceptional SERS activity with any plasmonic NPs (or) plasmonic plating for any analyte molecules. To confirm these activities, the Au NPs with a mean size of ∼10 nm were deposited on all six LINEPSS substrates and the Raman spectra of MB were collected from

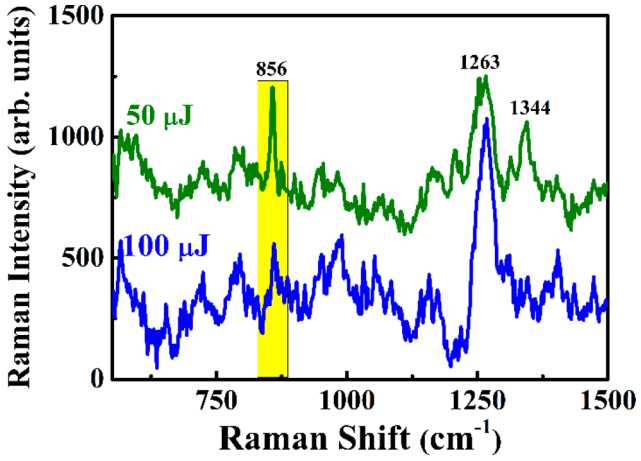


**Figure 8.** SERS spectra of DNT ($10^{-6}$ M) absorbed on Ag NPs coated LINEPSS substrates with different periodicity of 130 ± 10 nm and 150 ± 5 nm recorded with a 785 nm portable Raman system with 5 mW of power, and the integration time was 5 s for each spectrum.

them. Later, Ag plating was deposited on the above-mentioned six LINEPSS substrates after perfect cleaning and sonication of the substrates. These substrates were again employed for recording the SERS spectra of 5-amino-3-nitro-l,2,4-triazole (ANTA) molecules. Figure 9 illustrates Raman spectra of MB

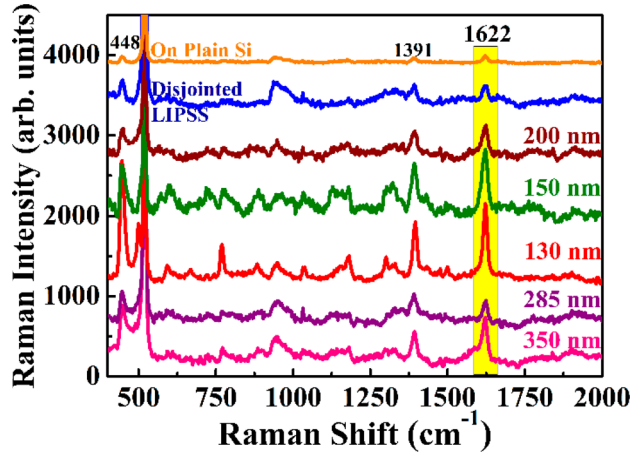


**Figure 9.** SERS spectra of MB ($10^{-7}$ M) absorbed on Au-NPs-coated LINEPSS substrates with different periodicity recorded with a 785 nm portable Raman system and using 5 mW of power, with an integration time of 5 s for each spectrum.

($10^{-7}$ M) recorded from six different substrates and the spectra revealed the prominent Raman bands, which are observed at 448, 1391, and 1622 $cm^{-1}$. The EF values that have been evaluated in this case for the characteristic mode (1622 $cm^{-1}$) are $2.5 \times 10^6$, $1.3 \times 10^6$, $4.6 \times 10^6$, $4 \times 10^6$, $1.8 \times 10^6$, and $1 \times 10^6$ for 350 ± 20 nm, 285 ± 15 nm, 130 ± 10 nm, 150 ± 5 nm, 200 ± 30 nm, and disjointed LIPSS, respectively. Figure 10 shows the recorded Raman spectra of molecules with a concentration of $1 \times 10^{-6}$ M on Ag-thin-film-coated LINEPSS substrates and 0.1 M on plain silicon wafer (reference spectrum), using a micro Raman spectrometer that had an excitation wavelength of 532 nm and an integration time of 0.5 s. It is evident that the Raman modes were largely enhanced on Ag-thin-film-coated LINEPSS substrates, compared with the modes on plain silicon at higher concentration of 0.1 M. The


DOI: 10.1021/acsomega.8b02629
ACS Omega 2018, 3, 18420−18432

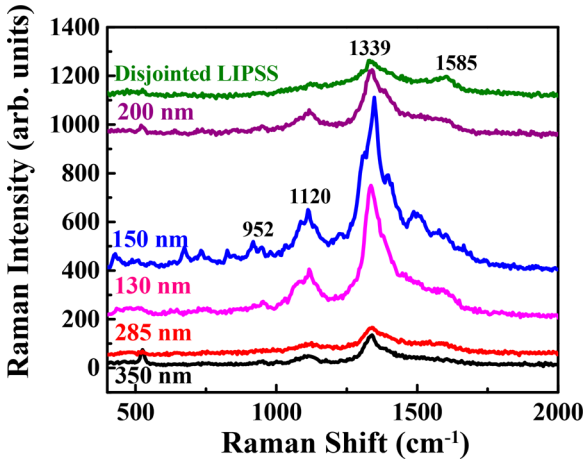


**Figure 10.** SERS spectra of ANTA ($10^{-6}$ M) absorbed on Ag-film-coated LINEPSS substrates with different periodicity recorded with a 532 nm micro Raman system with 1 mW of power and an integration time of 0.5 s for each spectrum.

peak at 1339 $cm^{-1}$ is assigned to the C−$NO_2$ symmetric stretch vibration, which can be termed as the characteristic mode of the molecule, while the other Raman modes observed at 952, 1125, and 1585 $cm^{-1}$ correspond to the N4−C5−N1 bending mode, the N−N symmetric stretching mode, and the C−$NH_2$ symmetrical stretch + $NH_2$ bend, respectively. The Raman intensity was observed to increase as the periodicity of LIPSS decreases from 350 ± 20 nm to 130 ± 10 nm. However, the Raman intensity decreased when the periodicity was further increased to 200 ± 30 nm and disjointed LIPSS. The size of formed Si NPs on LIPSS might also have played a significant role to add their contribution in Raman intensity enhancement. We believe that a small percentage of molecules (<40%) in the hot spots contributed to enhanced Raman intensity. To explore the enhancement capability of Ag metal plating Si NSs, the EF values were evaluated by comparing the SERS intensity with normal Raman intensity. Based on the intensities of the characteristic peak at 1339 $cm^{-1}$ in all SERS spectra, the EF values were estimated to be ∼1.2 × $10^7$, ∼1.3 × $10^7$, ∼2 × $10^7$, ∼5.32 × $10^7$, ∼2.5 × $10^7$, and ∼1.4 × $10^7$ for different periodicity of LINEPSS (350 ± 20 nm, 285 ± 15 nm, 130 ± 10 nm, 150 ± 5 nm, 200 ± 30 nm, and disjointed LIPSS, respectively). Our SERS data unambiguously revealed that the Ag metal plating on LINEPSS possesses potential for detecting the Raman modes of ANTA analyte with larger enhancement, and this might be ascribed to a large amplification of the local electric field, which is due to the combination of localized surface plasmons and propagating surface plasmons produced from the surfaces of spherical NPs and contribution from the periodic surface structures, respectively. The outcomes obtained from these studies demonstrate that laser-produced nanoparticle-embedded LIPSS substrates covered with Ag/Au nanoparticles and Ag thin film acquire efficient SERS reproducibility and stability, even though SERS studies were performed on various days, which were a few months apart. There is further scope for improvement in the performance of these structures, following the optimization of the Ag coating thickness and the periodicity of the gratings achieved. Furthermore, a combination of NPs and NSs is also expected to advance the detection capability (sensitivity). However, detailed studies are essential toward achieving this.

## CONCLUSIONS

A suitable liquid-assisted fs laser ablation technique has been used to investigate reproducible SERS substrates with multiple utility, because of their stability, uniformity, and strong enhancement in the Raman signal. In this work, laser-induced nanoparticle-embedded periodic structures (LINEPSS) were fabricated by fs laser ablation of silicon in acetone at different laser fluences. The obtained LIPSS with different sizes utilized for SERS measurements in this study were 350 ± 20 nm, 285 ± 15 nm, 130 ± 10 nm, 150 ± 5 nm, 200 ± 30 nm, and disjointed LIPSS, and the sizes of the Si nanoparticles embedded on the surface of LIPSS are no NPs, ∼150 nm, ∼90 nm, ∼67 nm, ∼135 nm, and ∼95 nm for 0.08 J/cm, 0.19 $J/cm^2$, 0.38 $J/cm^2$, 0.75 $J/cm^2$, 1.5 $J/cm^2$, and 3 $J/cm^2$, respectively. The efficient SERS substrates were then achieved by the deposition of Ag/Au nanoparticles on the surface of nanoparticle-embedded laser-induced periodic structures and they can create multiple hotspots. By employing the stable and reproducible Ag NPs deposited SERS-active substrate to the Raman studies of MB ($10^{-9}$ M) molecule, the highest EF value for MB at 1620 $cm^{-1}$ was determined to be 1.5 × $10^8$ with good reproducibility throughout the LINEPSS substrate (<8%). It was observed that the EF value for the DNT molecule ($10^{-6}$ M), ∼$10^5$, was achieved for Ag-NPs-deposited SERS-active substrates through simple cleaning processes. Similarly, Au-NPs-deposited LINEPSS substrates also produced enhanced Raman signal for MB molecule ($10^{-7}$ M) and the EF value was ∼$10^6$. In addition to that, Ag plating on the LINEPSS substrate can generate localized and propagating surface plasmons, which enhanced the Raman spectra of ANTA molecule (∼$10^{-6}$ M) and demonstrate the average EF value of ∼$10^7$. The strategy of our LINEPSSS fabrication succeeded in the resulting high reproducibility, along with superior Raman signal enhancements. Our future endeavor would be to prepare robust SERS targets that could detect most common explosives at trace concentrations, using a portable/hand-held Raman spectrometer, along with the capability to detect a variety of explosive molecules.

## EXPERIMENTAL DETAILS

The experimental schematic of ultrashort pulse laser ablation for LINEPSS fabrication is shown in Figure 1. Nanoparticle embedded LIPSS have been achieved in a single-step fs ablation process on *p*-type crystalline Si (100) substrate in liquid media. These experiments were performed using 1 kHz chirped pulse amplified Ti:sapphire laser system (LIBRA, M/s Coherent, USA) delivering nearly bandwidth limited laser pulses of ∼50 fs pulse width at 800 nm. The average power from the amplifier was ∼4 W. The laser beam was focused on the Si target, which was submerged in acetone in a Pyrex cell, and the effective thickness of liquid layer above the target was ∼5 mm. The Si targets were cleaned in an ultrasonic cleaner with acetone to remove the impurities before ablation. The refractive index and thickness of liquid layer play a crucial role in affecting the laser fluence at the focus on the surface of target. Consequently, the position of the focal plane shifts toward the target, which modifies the beam waist on the target surface. Moreover, the focal plane can shift, depending on the liquid media and height of the liquid from the target surface. To avoid this shift, we followed a strategy. First, we adjusted the focal plane exactly on the target surface in air by listening to the furious sound and observing the light produced by laser-



DOI: 10.1021/acsomega.8b02629
ACS Omega 2018, 3, 18420−18432

induced plasma. The modification of beam waist resulted in deposition of lesser fluence on the target. Second, we evaluated the shift (distance) of the focal plane by following the Menendez et al.[92] procedure under the effect of the refractive index ($n$) of the liquid media and height of the liquid layer from the surface of the target ($h$), by following the procedure mentioned in the previous research.[6] There is one more complexity behind the beam waist diameter ($2\omega_0$) at focus on the target, which plays a significant role in the mechanism of ablation. The produced beam waist on the target in liquid media is considerably larger than the beam waist generated in air. The increase in size of the beam waist on the target in liquid media could be due to the naturally existing nanoroughness ($\lambda/10$ or $\lambda/12$) of the metal/semiconductor/dielectric materials (target). The estimated effective spot size on the target surface was ∼140 $\mu$m, using the above-mentioned process. The combination of a half wave plate and a Brewster polarizer was utilized to control pulse energy and polarization direction of the laser beam. In this study, the typical fluences used were 0.08 J/cm$^2$, 0.19 J/cm$^2$, 0.38 J/cm$^2$, 0.75 J/cm$^2$, 1.5 J/cm$^2$, and 3 J/cm$^2$. The Pyrex cell, along with the submerged Si substrate in acetone, is fixed on a Nanodirect (Model NTS-25) three-dimensional stage and has a resolution of 25 nm, which is connected to the controller. The $X-Y$ stages were utilized to scan in such a way as to draw periodic lines with 100 $\mu$m spacing using scanning speeds of ∼0.2 and 0.5 mm/s in the $X$- and $Y$-directions, respectively. The time duration for ablation of every sample was 0.50 h. The complete details of fs laser ablation in liquids were reported in our earlier articles.[21,93] After the ablation, the substrates were sonicated and stored in safest place. The morphology of patterns formed on the crystalline Si substrates and elemental compositions were characterized by FESEM [Ultra 55 from Carl ZEISS instrument] technique energy-dispersive X-ray analysis and Raman spectroscopy using a WITec Alpha 300 spectrometer.

SERS measurements on these substrates were performed by using two Raman systems. In the case of bulk Raman system, the SERS studies were performed using a portable Raman spectrometer (B&W Tek, USA) with a continuous laser operated at a 785 nm wavelength and the laser power used was 5 mW. The substrates were prepared through drop casting of Ag/Au NP colloids on ablated Si substrates and incubated for half an hour to dry the sample at room temperature and, later, analyte molecules (∼2 $\mu$L) were placed on the dried Ag/Au-Si substrates. The Ag/Au-deposited Si patterned substrates were characterized by EDAX analysis. In the micro-Raman studies, a WITec Alpha 300 spectrometer was utilized to perform SERS studies at an excitation wavelength of 532 nm (cw). The SERS-active substrates were then prepared by ion beam deposition. Ag thin films were deposited on ablated Si substrates in a home-built ion beam deposition system evacuated by a turbo molecular pump (TMP). The dc ion source (DC25 Oxford Applied Research, U.K.) was a Kaufmann-type ion source capable of producing ion beams of 2.5 cm in diameter with a maximum beam energy of 1.5 keV. The ions were extracted and accelerated by applying a suitable potential to a dual-grid ion extraction system. Cathode current was maintained at 10 m Amp with an ion beam energy of 80 eV and an extraction voltage of −40 V. The deposition chamber was evacuated to a base pressure of $2 \times 10^{-6}$ Torr before introducing argon gas into the system. The pressure during deposition was $3 \times 10^{-3}$ Torr. A 3-in. diameter and 4-mm-thick Ag target was kept at 45° to the incident ion-beam direction. The substrates were held at room temperature during deposition, and substrates are mounted on a substrate holder, which was 8 cm from the target at a 45° angle and in the source axis. Acceleration voltage, cathode current, deposition pressure, and extraction voltages were well-calibrated to reach a deposition rate of 2 nm/min. The deposition was performed for 10 min to reach ∼20-nm-thick films on all the ablated Si substrates and was confirmed from the EDAX data.

## AUTHOR INFORMATION


### Corresponding Author

*E-mails: soma_venu@uohyd.ac.in, soma_venu@yahoo.com.

### ORCID

Venugopal Rao Soma: 0000-0001-5361-7256

### Present Addresses

[▽]Department of Physics, School of Physical Sciences, Sikkim University, sixth mile Samdur, 737102, Sikkim, India.
[#]Department of Electronics and Physics, GITAM (Deemed to be University), Visakhapatnam 530045, Andhra Pradesh, India.
[⊥]Department of Science and Humanities, National Institute of Technology Andhra Pradesh, Tadepalligudem 534 101, Andhra Pradesh, India.


### Author Contributions

S.H., S.S.B.M., and Y.B. have performed the laser ablation experiments and analyzed the nanoparticles and nanostructures obtained. S.H., S.S.B.M., and M.A.M. have performed the Raman measurements and analyzed the Raman data. V.R.S. supervised all of the research, from concept to final analysis. S.H., G.K.P., and V.R.S. were involved in writing the manuscript. All the authors have given their approval to the final version of the manuscript.


### Funding

Funding provided by DRDO, India through Grant No. ERIP/ER/1501138/M/01/319/D(R&D).


### Notes

The authors declare no competing financial interest.

## ACKNOWLEDGMENTS

S.H. acknowledges CSIR for Research Associateship and V.R.S. acknowledges DRDO for financial assistance and CNF, UoH for the Raman facility.

## ABBREVIATIONS

EF, enhancement factor; fs, femtosecond; LIPSS, laser-induced periodic surface structures; LINEPSS, laser-induced nanoparticle embedded in periodic surface structures; Ag/Au, silver/gold; SERS, surface enhanced Raman scattering

## REFERENCES


(1) Ross, G. The public health implications of polychlorinated biphenyls (PCBs) in the environment. *Ecotoxicol. Environ. Saf.* **2004**, *59* (3), 275−291.

(2) Ohtsubo, Y.; Kudo, T.; Tsuda, M.; Nagata, Y. Strategies for bioremediation of polychlorinated biphenyls. *Appl. Microbiol. Biotechnol.* **2004**, *65* (3), 250−258.

(3) Cicchetti, D. V.; Kaufman, A. S.; Sparrow, S. S. The relationship between prenatal and postnatal exposure to polychlorinated biphenyls (PCBs) and cognitive, neuropsychological, and behavioral deficits: A critical appraisal. *Psychology in the Schools* **2004**, *41* (6), 589−624.

(4) Hong, J. E.; Pyo, H.; Park, S.-J.; Lee, W. Determination of hydroxy-PCBs in urine by gas chromatography/mass spectrometry




DOI: 10.1021/acsomega.8b02629
*ACS Omega* 2018, 3, 18420−18432

with solid-phase extraction and derivatization. *Anal. Chim. Acta* **2005**, *531* (2), 249−256.
(5) Fleischmann, M.; Hendra, P. J.; McQuillan, A. J. Raman spectra of pyridine adsorbed at a silver electrode. *Chem. Phys. Lett.* **1974**, *26* (2), 163−166.
(6) Kneipp, K.; Wang, Y.; Kneipp, H.; Perelman, L. T.; Itzkan, I.; Dasari, R. R.; Feld, M. S. Single molecule detection using surface-enhanced Raman scattering (SERS). *Phys. Rev. Lett.* **1997**, *78* (9), 1667.
(7) Nie, S.; Emory, S. R. Probing single molecules and single nanoparticles by surface-enhanced Raman scattering. *Science* **1997**, *275* (5303), 1102−1106.
(8) Strehle, K. R.; Cialla, D.; Rösch, P.; Henkel, T.; Köhler, M.; Popp, J. A reproducible surface-enhanced Raman spectroscopy approach. Online SERS measurements in a segmented microfluidic system. *Anal. Chem.* **2007**, *79* (4), 1542−1547.
(9) Bandarenka, H. V.; Girel, K. V.; Zavatski, S. A.; Panarin, A.; Terekhov, S. N. Progress in the Development of SERS-Active Substrates Based on Metal-Coated Porous Silicon. *Materials* **2018**, *11* (5), 852.
(10) Novara, C.; Dalla Marta, S.; Virga, A.; Lamberti, A.; Angelini, A.; Chiadò, A.; Rivolo, P.; Geobaldo, F.; Sergo, V.; Bonifacio, A.; Giorgis, F. SERS-active Ag nanoparticles on porous silicon and PDMS substrates: a comparative study of uniformity and Raman efficiency. *J. Phys. Chem. C* **2016**, *120* (30), 16946−16953.
(11) Jeon, H. C.; Jeon, T. Y.; Shim, T. S.; Yang, S. M. Direct fabrication of hexagonally ordered ridged nanoarchitectures via dual interference lithography for efficient sensing applications. *Small* **2014**, *10* (8), 1490−1494.
(12) Yokota, Y.; Ueno, K.; Misawa, H. Highly Controlled Surface-Enhanced Raman Scattering Chips Using Nanoengineered Gold Blocks. *Small* **2011**, *7* (2), 252−258.
(13) Hsu, C.-H.; Lo, H.-C.; Chen, C.-F.; Wu, C. T.; Hwang, J.-S.; Das, D.; Tsai, J.; Chen, L.-C.; Chen, K.-H. Generally applicable self-masked dry etching technique for nanotip array fabrication. *Nano Lett.* **2004**, *4* (3), 471−475.
(14) Robatjazi, H.; Bahauddin, S. M.; Macfarlan, L. H.; Fu, S.; Thomann, I. Ultrathin AAO membrane as a generic template for sub-100 nm nanostructure fabrication. *Chem. Mater.* **2016**, *28* (13), 4546−4553.
(15) Vendamani, V.; Nageswara Rao, S.; Venugopal Rao, S.; Kanjilal, D.; Pathak, A. Three-dimensional hybrid silicon nanostructures for surface enhanced Raman spectroscopy based molecular detection. *J. Appl. Phys.* **2018**, *123* (1), 014301.
(16) Yang, J.; Li, J.; Du, Z.; Gong, Q.; Teng, J.; Hong, M. Laser hybrid micro/nano-structuring of Si surfaces in air and its applications for SERS detection. *Sci. Rep.* **2015**, *4*, 6657.
(17) Ben-Jaber, S.; Peveler, W. J.; Quesada-Cabrera, R.; Sol, C. W.; Papakonstantinou, I.; Parkin, I. P. Sensitive and specific detection of explosives in solution and vapour by surface-enhanced Raman spectroscopy on silver nanocubes. *Nanoscale* **2017**, *9* (42), 16459−16466.
(18) Hakonen, A.; Andersson, P. O.; Schmidt, M. S.; Rindzevicius, T.; Käll, M. Explosive and chemical threat detection by surface-enhanced Raman scattering: A review. *Anal. Chim. Acta* **2015**, *893*, 1−13.
(19) Olson, A. P.; Spies, K. B.; Browning, A. C.; Soneral, P. A.; Lindquist, N. C. Chemically imaging bacteria with super-resolution SERS on ultra-thin silver substrates. *Sci. Rep.* **2017**, *7* (1), 9135.
(20) Krishna Podagatlapalli, G.; Hamad, S.; Tewari, S. P.; Sreedhar, S.; Prasad, M. D.; Venugopal Rao, S. Silver nano-entities through ultrafast double ablation in aqueous media for surface enhanced Raman scattering and photonics applications. *J. Appl. Phys.* **2013**, *113* (7), 073106.
(21) Hamad, S.; Podagatlapalli, G. K.; Mohiddon, M. A.; Soma, V. R. Cost effective nanostructured copper substrates prepared with ultrafast laser pulses for explosives detection using surface enhanced Raman scattering. *Appl. Phys. Lett.* **2014**, *104* (26), 263104.
(22) Nguyen, T. B.; Thu Vu, T. K.; Nguyen, Q. D.; Nguyen, T. D.; Nguyen, T. A.; Trinh, T. H. Preparation of metal nanoparticles for surface enhanced Raman scattering by laser ablation method. *Adv. Nat. Sci.: Nanosci. Nanotechnol.* **2012**, *3* (2), 025016.
(23) Herrera, G. M.; Padilla, A. C.; Hernandez-Rivera, S. P. Surface enhanced Raman scattering (SERS) studies of gold and silver nanoparticles prepared by laser ablation. *Nanomaterials* **2013**, *3* (1), 158−172.
(24) Jin, Y.; Wang, Y.; Chen, M.; Xiao, X.; Zhang, T.; Wang, J.; Jiang, K.; Fan, S.; Li, Q. Highly Sensitive, Uniform, and Reproducible Surface-Enhanced Raman Spectroscopy Substrate with Nanometer-Scale Quasi-periodic Nanostructures. *ACS Appl. Mater. Interfaces* **2017**, *9* (37), 32369−32376.
(25) Bezares, F. J.; Caldwell, J. D.; Glembocki, O.; Rendell, R. W.; Feygelson, M.; Ukaegbu, M.; Kasica, R.; Shirey, L.; Bassim, N. D.; Hosten, C. The role of propagating and localized surface plasmons for SERS enhancement in periodic nanostructures. *Plasmonics* **2012**, *7* (1), 143−150.
(26) Tao, W.; Zhao, A.; Sun, H.; Gan, Z.; Zhang, M.; Li, D.; Guo, H. Periodic silver nanodishes as sensitive and reproducible surface-enhanced Raman scattering substrates. *RSC Adv.* **2014**, *4* (7), 3487−3493.
(27) Farcau, C.; Astilean, S. Periodically nanostructured substrates for surface enhanced Raman spectroscopy. *J. Mol. Struct.* **2014**, *1073*, 102−111.
(28) Beermann, J.; Novikov, S. M.; Leosson, K.; Bozhevolnyi, S. I. Surface enhanced Raman imaging: periodic arrays and individual metal nanoparticles. *Opt. Express* **2009**, *17* (15), 12698−12705.
(29) Linn, N. C.; Sun, C.-H.; Arya, A.; Jiang, P.; Jiang, B. Surface-enhanced Raman scattering on periodic metal nanotips with tunable sharpness. *Nanotechnology* **2009**, *20* (22), 225303.
(30) Zhao, W.; Liu, X.; Xu, Y.; Wang, S.; Sun, T.; Liu, S.; Wu, X.; Xu, Z. Polymer nanopillar array with Au nanoparticle inlays as a flexible and transparent SERS substrate. *RSC Adv.* **2016**, *6* (42), 35527−35531.
(31) Zhang, C.; Yi, P.; Peng, L.; Lai, X.; Chen, J.; Huang, M.; Ni, J. Continuous fabrication of nanostructure arrays for flexible surface enhanced Raman scattering substrate. *Sci. Rep.* **2017**, *7*, 39814.
(32) Cunha, A.; Zouani, O. F.; Plawinski, L.; Botelho do Rego, A. M.; Almeida, A.; Vilar, R.; Durrieu, M.-C. Human mesenchymal stem cell behavior on femtosecond laser-textured Ti-6Al-4V surfaces. *Nanomedicine* **2015**, *10* (5), 725−739.
(33) Györgyey, A.; Ungvári, K.; Kecskeméti, G.; Kopniczky, J.; Hopp, B.; Oszkó, A.; Pelsöczi, I.; Rakonczay, Z.; Nagy, K.; Turzó, K. Attachment and proliferation of human osteoblast-like cells (MG-63) on laser-ablated titanium implant material. *Mater. Sci. Eng., C* **2013**, *33* (7), 4251−4259.
(34) Martínez-Calderon, M.; Manso-Silván, M.; Rodríguez, A.; Gómez-Aranzadi, M.; García-Ruiz, J.; Olaizola, S.; Martín-Palma, R. Surface micro-and nano-texturing of stainless steel by femtosecond laser for the control of cell migration. *Sci. Rep.* **2016**, *6*, 36296.
(35) Granados, E.; Calderon, M. M.; Krzywinski, J.; Wörner, E.; Rodriguez, A.; Aranzadi, M. G.; Olaizola, S. M. Enhancement of surface area and wettability properties of boron doped diamond by femtosecond laser-induced periodic surface structuring. *Opt. Mater. Express* **2017**, *7* (9), 3389−3396.
(36) Martinez-Vazquez, R.; Osellame, R.; Cerullo, G.; Ramponi, R.; Svelto, O. Fabrication of photonic devices in nanostructured glasses by femtosecond laser pulses. *Opt. Express* **2007**, *15* (20), 12628−12635.
(37) Vorobyev, A.; Makin, V.; Guo, C. Periodic ordering of random surface nanostructures induced by femtosecond laser pulses on metals. *J. Appl. Phys.* **2007**, *101* (3), 034903.
(38) Golosov, E.; Ionin, A.; Kolobov, Y. R.; Kudryashov, S.; Ligachev, A.; Makarov, S.; Novoselov, Y. N.; Seleznev, L.; Sinitsyn, D. Formation of periodic nanostructures on aluminum surface by femtosecond laser pulses. *Nanotechnol. Russ.* **2011**, *6* (3−4), 237−243.
(39) Sakabe, S.; Hashida, M.; Tokita, S.; Namba, S.; Okamuro, K. Mechanism for self-formation of periodic grating structures on a metal


DOI: 10.1021/acsomega.8b02629
*ACS Omega* 2018, 3, 18420−18432

surface by a femtosecond laser pulse. *Phys. Rev. B: Condens. Matter Mater. Phys.* **2009**, *79* (3), 033409.
(40) Bonse, J.; Rosenfeld, A.; Krüger, J. On the role of surface plasmon polaritons in the formation of laser-induced periodic surface structures upon irradiation of silicon by femtosecond-laser pulses. *J. Appl. Phys.* **2009**, *106* (10), 104910.
(41) Hamad, S.; Podagatlapalli, G. K.; Vendamani, V.; Nageswara Rao, S.; Pathak, A.; Tewari, S. P.; Venugopal Rao, S. Femtosecond ablation of silicon in acetone: tunable photoluminescence from generated nanoparticles and fabrication of surface nanostructures. *J. Phys. Chem. C* **2014**, *118* (13), 7139−7151.
(42) Hsu, E.; Crawford, T.; Tiedje, H.; Haugen, H. Periodic surface structures on gallium phosphide after irradiation with 150 fs−7 ns laser pulses at 800 nm. *Appl. Phys. Lett.* **2007**, *91* (11), 111102.
(43) Ashkenasi, D.; Rosenfeld, A.; Varel, H.; Wähmer, M.; Campbell, E. Laser processing of sapphire with picosecond and sub-picosecond pulses. *Appl. Surf. Sci.* **1997**, *120* (1−2), 65−80.
(44) Reif, J.; Costache, F.; Henyk, M.; Pandelov, S. V. Ripples revisited: non-classical morphology at the bottom of femtosecond laser ablation craters in transparent dielectrics. *Appl. Surf. Sci.* **2002**, *197*, 891−895.
(45) Rohloff, M.; Das, S.; Höhm, S.; Grunwald, R.; Rosenfeld, A.; Krüger, J.; Bonse, J. Formation of laser-induced periodic surface structures on fused silica upon multiple cross-polarized double-femtosecond-laser-pulse irradiation sequences. *J. Appl. Phys.* **2011**, *110* (1), 014910.
(46) He, X.; Datta, A.; Nam, W.; Traverso, L. M.; Xu, X. Sub-diffraction limited writing based on laser induced periodic surface structures (LIPSS). *Sci. Rep.* **2016**, *6*, 35035.
(47) Fuentes-Edfuf, Y.; Garcia-Lechuga, M.; Puerto, D.; Florian, C.; Garcia-Leis, A.; Sanchez-Cortes, S.; Solis, J.; Siegel, J. Author Correction: Coherent scatter-controlled phase-change grating structures in silicon using femtosecond laser pulses. *Sci. Rep.* **2018**, *8* (1), 6135.
(48) Nivas, J. J. J.; He, S.; Rubano, A.; Vecchione, A.; Paparo, D.; Marrucci, L.; Bruzzese, R.; Amoruso, S. Direct femtosecond laser surface structuring with optical vortex beams generated by a q-plate. *Sci. Rep.* **2016**, *5*, 17929.
(49) Höhm, S.; Rosenfeld, A.; Krüger, J.; Bonse, J. Laser-induced periodic surface structures on titanium upon single-and two-color femtosecond double-pulse irradiation. *Opt. Express* **2015**, *23* (20), 25959−25971.
(50) Fadeeva, E.; Chichkov, B. Biomimetic Liquid-Repellent Surfaces by Ultrafast Laser Processing. *Appl. Sci.* **2018**, *8* (9), 1424.
(51) Gnilitskyi, I.; Derrien, T. J.-Y.; Levy, Y.; Bulgakova, N. M.; Mocek, T.; Orazi, L. High-speed manufacturing of highly regular femtosecond laser-induced periodic surface structures: physical origin of regularity. *Sci. Rep.* **2017**, *7* (1), 8485.
(52) Bonse, J.; Krüger, J.; Höhm, S.; Rosenfeld, A. Femtosecond laser-induced periodic surface structures. *J. Laser Appl.* **2012**, *24* (4), 042006.
(53) Bonse, J.; Höhm, S.; Kirner, S. V.; Rosenfeld, A.; Krüger, J. Laser-induced periodic surface structures—a scientific evergreen. *IEEE J. Sel. Top. Quantum Electron.* **2017**, *23* (3), 109−123.
(54) Birnbaum, M. Semiconductor surface damage produced by ruby lasers. *J. Appl. Phys.* **1965**, *36* (11), 3688−3689.
(55) He, S.; Nivas, J. J.; Anoop, K.; Vecchione, A.; Hu, M.; Bruzzese, R.; Amoruso, S. Surface structures induced by ultrashort laser pulses: Formation mechanisms of ripples and grooves. *Appl. Surf. Sci.* **2015**, *353*, 1214−1222.
(56) Sipe, J.; Young, J. F.; Preston, J.; Van Driel, H. Laser-induced periodic surface structure. I. Theory. *Phys. Rev. B: Condens. Matter Mater. Phys.* **1983**, *27* (2), 1141.
(57) Derrien, T.-Y.; Torres, R.; Sarnet, T.; Sentis, M.; Itina, T. E. Formation of femtosecond laser induced surface structures on silicon: Insights from numerical modeling and single pulse experiments. *Appl. Surf. Sci.* **2012**, *258* (23), 9487−9490.
(58) Zhang, W.; Cheng, G.; Feng, Q. Unclassical ripple patterns in single-crystal silicon produced by femtosecond laser irradiation. *Appl. Surf. Sci.* **2012**, *263*, 436−439.
(59) Reif, J.; Martens, C.; Uhlig, S.; Ratzke, M.; Varlamova, O.; Valette, S.; Benayoun, S. On large area LIPSS coverage by multiple pulses. *Appl. Surf. Sci.* **2015**, *336*, 249−254.
(60) Höhm, S.; Herzlieb, M.; Rosenfeld, A.; Krüger, J.; Bonse, J. Dynamics of the formation of laser-induced periodic surface structures (LIPSS) upon femtosecond two-color double-pulse irradiation of metals, semiconductors, and dielectrics. *Appl. Surf. Sci.* **2016**, *374*, 331−338.
(61) Fraggelakis, F.; Stratakis, E.; Loukakos, P. Control of periodic surface structures on silicon by combined temporal and polarization shaping of femtosecond laser pulses. *Appl. Surf. Sci.* **2018**, *444*, 154−160.
(62) Garcia-Lechuga, M.; Puerto, D.; Fuentes-Edfuf, Y.; Solis, J.; Siegel, J. Ultrafast moving-spot microscopy: Birth and growth of laser-induced periodic surface structures. *ACS Photonics* **2016**, *3* (10), 1961−1967.
(63) Keilmann, F.; Bai, Y. Periodic surface structures frozen into CO2 laser-melted quartz. *Appl. Phys. A: Solids Surf.* **1982**, *29* (1), 9−18.
(64) Wang, J.; Guo, C. Numerical study of ultrafast dynamics of femtosecond laser-induced periodic surface structure formation on noble metals. *J. Appl. Phys.* **2007**, *102* (5), 053522.
(65) Almeida, G.; Martins, R.; Otuka, A.; Siqueira, J.; Mendonca, C. Laser induced periodic surface structuring on Si by temporal shaped femtosecond pulses. *Opt. Express* **2015**, *23* (21), 27597−27605.
(66) Bonse, J.; Krüger, J. Pulse number dependence of laser-induced periodic surface structures for femtosecond laser irradiation of silicon. *J. Appl. Phys.* **2010**, *108* (3), 034903.
(67) Wang, J.; Jia, Z.; Lv, C. Enhanced Raman scattering in porous silicon grating. *Opt. Express* **2018**, *26* (6), 6507−6518.
(68) Han, Y.; Lan, X.; Wei, T.; Tsai, H.-L.; Xiao, H. Surface enhanced Raman scattering silica substrate fast fabrication by femtosecond laser pulses. *Appl. Phys. A: Mater. Sci. Process.* **2009**, *97* (3), 721.
(69) Zhu, Z.; Yan, Z.; Zhan, P.; Wang, Z. Large-area surface-enhanced Raman scattering-active substrates fabricated by femtosecond laser ablation. *Sci. China: Phys., Mech. Astron.* **2013**, *56* (9), 1806−1809.
(70) Harilal, S. S.; Freeman, J. R.; Diwakar, P. K.; Hassanein, A., Femtosecond laser ablation: Fundamentals and applications. In *Laser-Induced Breakdown Spectroscopy*; Springer: 2014; pp 143−166.
(71) Chichkov, B. N.; Momma, C.; Nolte, S.; von Alvensleben, F.; Tünnermann, A. Femtosecond, picosecond and nanosecond laser ablation of solids. *Appl. Phys. A: Mater. Sci. Process.* **1996**, *63* (2), 109−115.
(72) Raether, H., Surface plasmons on gratings. In *Surface Plasmons on Smooth and Rough Surfaces and on Gratings*; Springer: 1988; pp 91−116.
(73) Miyaji, G.; Miyazaki, K.; Zhang, K.; Yoshifuji, T.; Fujita, J. Mechanism of femtosecond-laser-induced periodic nanostructure formation on crystalline silicon surface immersed in water. *Opt. Express* **2012**, *20* (14), 14848−14856.
(74) Huang, M.; Zhao, F.; Cheng, Y.; Xu, N.; Xu, Z. Origin of laser-induced near-subwavelength ripples: interference between surface plasmons and incident laser. *ACS Nano* **2009**, *3* (12), 4062−4070.
(75) Derrien, T.-Y.; Koter, R.; Krüger, J.; Höhm, S.; Rosenfeld, A.; Bonse, J. Plasmonic formation mechanism of periodic 100-nm-structures upon femtosecond laser irradiation of silicon in water. *J. Appl. Phys.* **2014**, *116* (7), 074902.
(76) Amendola, V.; Meneghetti, M. What controls the composition and the structure of nanomaterials generated by laser ablation in liquid solution? *Phys. Chem. Chem. Phys.* **2013**, *15* (9), 3027−3046.
(77) Suslick, K. S.; Flannigan, D. J. Inside a collapsing bubble: sonoluminescence and the conditions during cavitation. *Annu. Rev. Phys. Chem.* **2008**, *59*, 659−683.



DOI: 10.1021/acsomega.8b02629
*ACS Omega* 2018, 3, 18420−18432

(78) Brennen, C. E. *Cavitation and Bubble Dynamics*. Oxford Engineering Science Series, No. *44*; Oxford University Press: New York, 1995.
(79) Wagener, P.; Ibrahimkutty, S.; Menzel, A.; Plech, A.; Barcikowski, S. Dynamics of silver nanoparticle formation and agglomeration inside the cavitation bubble after pulsed laser ablation in liquid. *Phys. Chem. Chem. Phys.* **2013**, *15* (9), 3068−3074.
(80) De Giacomo, A.; Dell'Aglio, M.; De Pascale, O.; Capitelli, M. From single pulse to double pulse ns-laser induced breakdown spectroscopy under water: elemental analysis of aqueous solutions and submerged solid samples. *Spectrochim. Acta, Part B* **2007**, *62* (8), 721−738.
(81) Tsuji, T.; Thang, D.-H.; Okazaki, Y.; Nakanishi, M.; Tsuboi, Y.; Tsuji, M. Preparation of silver nanoparticles by laser ablation in polyvinylpyrrolidone solutions. *Appl. Surf. Sci.* **2008**, *254* (16), 5224−5230.
(82) De Giacomo, A.; De Bonis, A.; Dell'Aglio, M.; De Pascale, O.; Gaudiuso, R.; Orlando, S.; Santagata, A.; Senesi, G.; Taccogna, F.; Teghil, R. Laser ablation of graphite in water in a range of pressure from 1 to 146 atm using single and double pulse techniques for the production of carbon nanostructures. *J. Phys. Chem. C* **2011**, *115* (12), 5123−5130.
(83) Berthe, L.; Fabbro, R.; Peyre, P.; Tollier, L.; Bartnicki, E. Shock waves from a water-confined laser-generated plasma. *J. Appl. Phys.* **1997**, *82* (6), 2826−2832.
(84) Moram, S. S. B.; Byram, C.; Shibu, S. N.; Chilukamarri, B. M.; Soma, V. R. Ag/Au Nanoparticle-Loaded Paper-Based Versatile Surface-Enhanced Raman Spectroscopy Substrates for Multiple Explosives Detection. *ACS Omega* **2018**, *3* (7), 8190−8201.
(85) Moram, S. S. B.; Byram, C.; Soma, V. R. Femtosecond Laser Fabricated Ag@ Au and Cu@ Au Alloy Nanoparticles for Surface Enhanced Raman Spectroscopy Based Trace Explosives Detection. *Front. Phys.* **2018**, *6*, 28.
(86) Olea-Mejía, O.; Fernández-Mondragón, M.; Rodríguez-de la Concha, G.; Camacho-López, M. SERS-active Ag, Au and Ag−Au alloy nanoparticles obtained by laser ablation in liquids for sensing methylene blue. *Appl. Surf. Sci.* **2015**, *348*, 66−70.
(87) Mikac, L.; Ivanda, M.; Gotić, M.; Maksimović, A.; Trusso, S.; D'Andrea, C.; Foti, A.; Irrera, A.; Fazio, B.; Gucciardi, P. G. Metal nanoparticles deposited on porous silicon templates as novel substrates for SERS. *Croat. Chem. Acta* **2015**, *88* (4), 437−444.
(88) Hamdorf, A.; Olson, M.; Lin, C.-H.; Jiang, L.; Zhou, J.; Xiao, H.; Tsai, H.-L. Femtosecond and nanosecond laser fabricated substrate for surface-enhanced Raman scattering. *Opt. Lett.* **2011**, *36* (17), 3353.
(89) Kuncicky, D. M.; Prevo, B. G.; Velev, O. D. Controlled assembly of SERS substrates templated by colloidal crystal films. *J. Mater. Chem.* **2006**, *16* (13), 1207−1211.
(90) Wells, S. M.; Retterer, S. D.; Oran, J. M.; Sepaniak, M. J. Controllable nanofabrication of aggregate-like nanoparticle substrates and evaluation for surface-enhanced Raman spectroscopy. *ACS Nano* **2009**, *3* (12), 3845−3853.
(91) Ben-Jaber, S.; Peveler, W. J.; Quesada-Cabrera, R.; Sol, C. W. O.; Papakonstantinou, I.; Parkin, I. P. Sensitive and specific detection of explosives in solution and vapour by surface-enhanced Raman spectroscopy on silver nanocubes. *Nanoscale* **2017**, *9* (42), 16459−16466.
(92) Menéndez-Manjón, A.; Wagener, P.; Barcikowski, S. Transfer-matrix method for efficient ablation by pulsed laser ablation and nanoparticle generation in liquids. *J. Phys. Chem. C* **2011**, *115* (12), 5108−5114.
(93) Podagatlapalli, G. K.; Hamad, S.; Sreedhar, S.; Tewari, S. P.; Venugopal Rao, S. Fabrication and characterization of aluminum nanostructures and nanoparticles obtained using femtosecond ablation technique. *Chem. Phys. Lett.* **2012**, *530*, 93−97.



DOI: 10.1021/acsomega.8b02629
*ACS Omega* 2018, 3, 18420−18432